Optics Letters

Generating six pairs of bandwidth-expanded entangled sideband modes via time delay compensation

Shaoping Shi,[1] Yimiao Wu,[1] Li Gao,[1] Li-ang Zheng,[1] Long Tian,[1,2,3] Yajun Wang,[1,2] Wei Li,[1,2] and Yaohui Zheng[1,2,*]

[1]State Key Laboratory of Quantum Optics and Quantum Optics Devices, Institute of Opto-Electronics, Shanxi University, Taiyuan 030006, China
[2]Collaborative Innovation Center of Extreme Optics, Shanxi University, Taiyuan, Shanxi 030006, China
[3]tianlong@sxu.edu.cn
*yhzheng@sxu.edu.cn

Received 14 April 2023; revised 10 May 2023; accepted 14 May 2023; posted 15 May 2023; published 1 June 2023

Quantum entanglement is an important pillar of quantum information processing. In addition to the entanglement degree, the bandwidth of entangled states becomes another focus of quantum communication. Here, by virtue of a broadband frequency-dependent beam splitter, we experimentally demonstrate six pairs of independent entangled sideband modes with maximum entanglement degree of 8.1 dB. Utilizing a time delay compensation scheme, the bandwidth of independent entangled sideband modes is expanded to dozens of megahertz. This work provides a valuable resource to implement efficient quantum information processing.

https://doi.org/10.1364/OL.493217

With the continual exploration by quantum physicists, quantum information protocols, such as quantum dense coding [1,2], quantum key distribution [3–5], and quantum teleportation [6–9], are moving gradually toward practical applications. Increasing channel number and enhancing capacity of each quantum channel to the largest extent are ongoing pursuits [10–12]. Here, we consider the creation of a squeezed state with an optical parametric oscillator (OPO), in which a pump photon of frequency $2\omega_0$ splits into a pair of lower-energy photons subject to energy conservation and the cavity resonance condition [13]. Each pair of symmetric sidebands around half the pump frequency ω_0 initiate quantum correlation [14,15], which makes the squeezed state exhibit fewer fluctuations than the shot noise limit (SNL) in one quadrature. Therefore, the squeezed state generated from a parametric downconversion process should intrinsically have a large bandwidth that covers the whole spectral acceptance range of nonlinear crystal [16]. However, the optical cavity introduces spectral filtering, which leads to a frequency-comb-type spectral distribution of the downconverted light [17,18]. These comb-teeth have a width that is the same as the linewidth of the OPO, having the separation of the cavity free spectral range (FSR).

At first, two narrowband upper and lower modes of a squeezed field were separated by employing a ring filter cavity (RFC) as frequency-dependent beam splitter, constructing Einstein–Podolsky–Rosen (EPR) sideband entanglement, and their correlations were detected with two balanced homodyne detectors (BHDs) that used frequency-shifted local oscillators (LOs) [19]. Later 15 pairs of quadripartite entangled states, 60 modes dual-rail cluster state were sequentially created using one OPO [20,21]. With an OPO driven by a femtosecond pulse train, the entanglement of all possible bipartitions among ten FSRs was demonstrated [22]. These demonstrations verify that entangled sideband modes have a large bandwidth that covers many FSRs of the OPO. In addition, a scheme that splits a single broadband squeezed field into N pairs of independent EPR sideband entanglement fields was also proposed, but not experimentally demonstrated for a long time [14,23]. Recently, we presented a frequency-comb-type control scheme of entangled sideband modes, solved the unmanageable problem of higher-order longitudinal modes, and produced many pairs of entangled sideband modes with high entanglement degree [24]. For practical quantum communication systems, the channel capacity is not only dependent on the entanglement degree, but also proportional to the bandwidth of the entanglement state [25]. However, owing to the additional phase delay originating from the transmission process of the RFC, the phase acquired by the transmission sideband modes is dependent on measurement frequency, leading to measured quadrature rotation with frequency [26–28]. Therefore, the generation of entangled sideband modes with larger bandwidth faces a challenge.

In this Letter, we propose a phase delay compensation scheme by virtue of additional time delay of the electrical signal, effectively expanding the bandwidth of each pair of entangled sideband modes. Utilizing the compensation scheme, we experimentally generate six pairs of entangled sideband modes with maximum entanglement degrees of 7.8, 8.1, 7.9, 8.0, 7.7, and 6.1 dB, respectively. Each pair of entangled modes is located at different resonances of the OPO, which intrinsically guarantees that these entangled modes have large frequency intervals and enough bandwidth. All these obtained entangled sideband modes have a bandwidth of more than 32 MHz, which is of

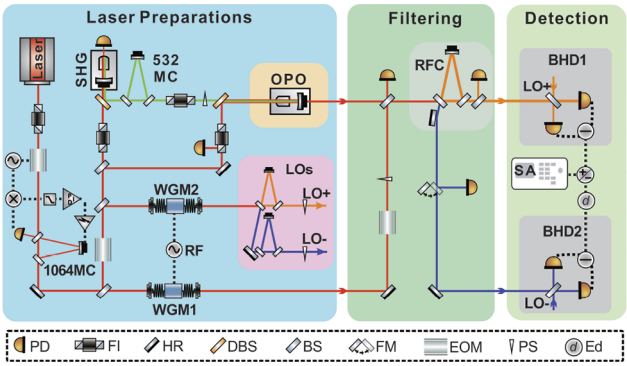

Fig. 1. Experimental setup of the high-order entangled sideband mode generation. MC, mode cleaner; SHG, second-harmonic generator; OPO, optical parametric oscillator; WGM, waveguide phase modulator; RF, radio frequency source; LO, local oscillator; RFC, ring filter cavity; BHD, balanced homodyne detector; SA, spectrum analyzer; PD, photodetector; FI, Faraday isolator; HR, high-reflection mirror; DBS, dichroic beam splitter; BS, beam splitter; FM, flip mirror; EOM, electro-optical modulator; PS, phase shifter; Ed, electronic delay.

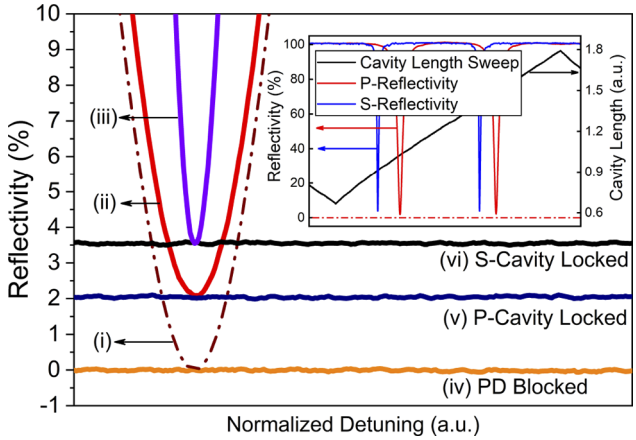

Fig. 2. Measurement results of RFC transmission loss for different polarization beams. Trace (i): theoretical reflection curve of the RFC with perfect impedance matching and mode matching. Trace (ii) and trace (iii): reflection signals of P- and S-polarization beam. Trace (iv): DC reference with the detector blocked. Trace (v) and trace (vi): DC signals with P- and S-polarization on resonance. The inset shows the unabridged FSR to infer the linewidth of the RFC.

vital importance for practical frequency-multiplexing quantum communication [10,11].

A schematic of our experimental setup is illustrated in Fig. 1. The squeezed state preparation, including spatial–temporal filtering, polarization purifying, pump beam generation, LO frequency shifting, and squeezed state generation, is similar to that of our previous works [24,29,30]. Different from the generation of a two-mode squeezed state [31–33], the entangled sideband modes are generated by separating the symmetrical sideband modes around the carrier mode. Since there are not enough coherent amplitudes at these sideband modes of an optical squeezed state, the extraction of these signals, which are needed for actively filtering the cavities and relative phases between LOs and signals in the downstream experiment, is impossible [34]. In order to solve the problem, a frequency-comb-type beam that is generated from a fiber coupled waveguide phase modulator (WGM) is employed as an auxiliary light control [24].

The RFC that adopts a triangular-shaped cavity design is located behind the OPO. The RFC resonates with upper sideband modes, while reflecting the rest, particularly the lower sidebands that are symmetric with the transmitted sidebands along half the pump frequency. The RFC has a FSR of 1.29 GHz and linewidth of 80 MHz, which can effectively separate the upper sideband modes from the corresponding lower sideband modes, not narrowing the bandwidth of the sideband modes. The separated sideband modes interfere with the corresponding LOs on a 50:50 beam splitter and directed toward two pairs of BHDs to measure the correlation noise [35].

To accurately evaluate the loss of entangled sideband modes in the separation process, we used a photodetector and oscilloscope to collect the reflection signals of the RFC of different polarized light fields [36,37], as shown in Fig. 2. The P-/S-polarization resonance modes of the RFC are non-degenerate due to the dispersion of the input/output coupling mirrors. We normalize them to the same resonant position for visual convenience. It can be inferred that the transmissivity and linewidth of the filter cavity of different polarized light fields are $\eta_{P(S)} = 98.0\%$ (96.5%) and $\Delta\nu_{P(S)} = 80$ MHz (24 MHz), respectively. Under the resonating and detuning conditions of the RFC, the squeezing noise variances measured at transmission and reflection ends of the RFC are 8.2 dB and 9.0 dB at the analysis frequency of 1 MHz without subtracting electronic noise. Considering that the squeezing level at the output of the OPO is 12.0 dB, we can infer that the transmission loss of the RFC is 2.7% [38]. The value of η decreases by the Lorenz function with the analysis frequency.

In addition to the loss, the separation process of entangled sideband modes also results in a time delay, which leads to the degradation of the quantum correlation that is dependent on the analysis frequency [26,28]. For a near-impedance-matching RFC, the additional time delay T of the transmission field is dependent on the Q factor of the RFC, which can be approximately expressed as [39,40]

$$T = \frac{2Q}{\omega_0}. \tag{1}$$

According to the expression $Q = \omega_0/(2\pi \times \Delta\nu)$ for the Q factor, T can be transformed into $T = 1/(\pi \times \Delta\nu)$ ($\Delta\nu$ is the cavity linewidth). By virtue of the measurement results of the RFC parameters above, T (3.9 ns for P-polarization, 13.2 ns for S-polarization) can be obtained.

For implementing BHDs on sideband modes, six pairs of frequency-shifting LOs are prepared by utilizing WGMs and subsequent optical mode cleaners. Each WGM is modulated by a radio frequency (RF) source with a frequency of approximately $\Omega_n = n \times \mathrm{FSR_{OPO}}$ (n is an integer, $\mathrm{FSR_{OPO}}$ is the FSR of the OPO). Before performing each measurement, we continuously tune the modulation frequency near Ω_n to optimize the correlation noise variances of sideband modes.

To confirm the effect of the time delay T, we first measure the correlation noise variances of first-order sideband modes. Figure 3 presents the measurement results for the analysis frequency range from 2 MHz to 10 MHz. With the signal ports of the two BHDs blocked, the output of the joint measurement corresponds to the SNL, shown in trace (i). Without delay compensation, the noise variances degrade with the analysis frequency, shown with trace (ii) for the P-polarization resonance mode of the RFC and trace (iii) for the S-polarization one. The

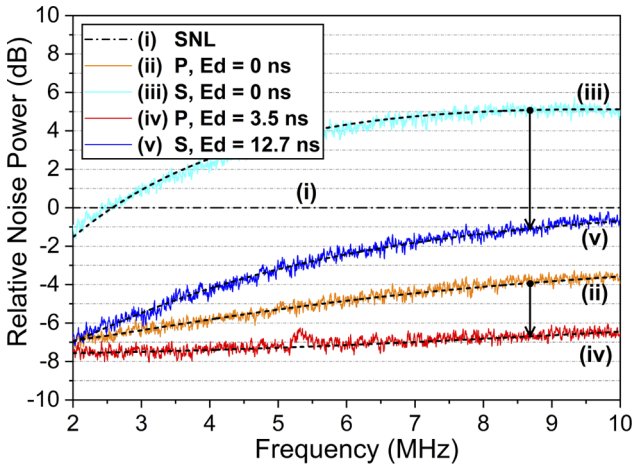

Fig. 3. Correlation noise variances of first sideband modes with P-polarization and S-polarization resonating, under the conditions of with and without delay compensation. The noise peak of trace (iv) at 5.3 MHz comes from the coupling of electronic noise.

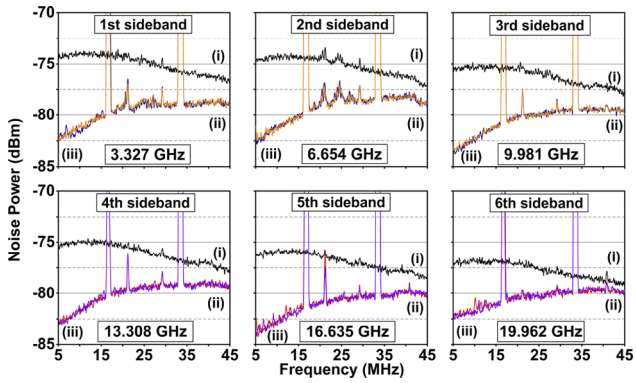

Fig. 4. Noise power spectra of quadrature amplitude sum and phase difference of six pairs of entangled sideband modes. The results are recorded at an analysis frequency from 5 MHz to 45 MHz, with a resolution bandwidth of 300 kHz and a video bandwidth of 200 Hz. Trace (i) is the SNL. Trace (ii) and trace (iii) represent the noise power of quadrature amplitude sum and phase difference, respectively.

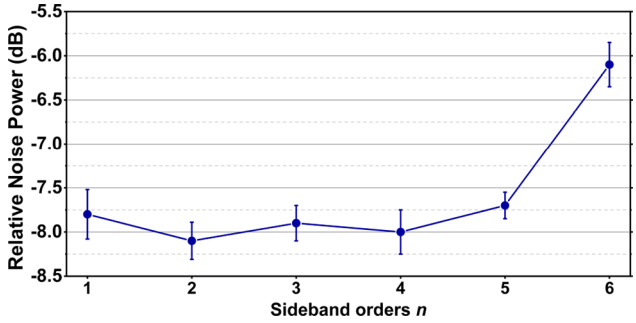

Fig. 5. Optimal correlation noise variances of the first- to sixth-order entangled sideband modes. The results are recorded at an analysis frequency of 1 MHz. The variances of quadrature amplitude sum and phase difference are unbiased and the distinction can be ignored.

sharp change of noise variances with the analysis frequency is mainly caused by the time delay T that originates from the RFC. With delay compensation through electronic delay at the output of BHD2, the bandwidth of the noise spectra is effectively optimized, shown with trace (iv) and trace (v). All of these dashed lines are the theoretical results. Owing to the narrower linewidth of the S-polarization resonance modes, there is a larger loss for the sideband field far away from the central one, degrading more severely the noise variances for the high-frequency band. It is worth noting that we employ different electronic delays to compensate the time delay T from S-polarization and P-polarization resonance modes. To achieve optimal compensation, the time delay introduced from the electronic delay should be equal to T of the RFC. Nevertheless, the electronic delay is 3.5 ns and 12.7 ns for P-polarization and S-polarization resonance modes of the RFC, respectively. The electronic delay has a slight difference from T of the RFC, which is mainly attributed to the measurement error. The results further confirm the dependence of T on the Q factor.

By tuning and optimizing the modulation frequency and the corresponding RF modulation power, we in turn obtain noise power spectra of quadrature amplitude sum and phase difference of the first- to sixth-order entangled sideband modes. The P-polarization resonance mode of the RFC has a linewidth of 80 MHz, which is more than the linewidth of the OPO (68 MHz). Thus, the separation process of the upper and lower sideband modes is performed by employing P-polarization resonance of the RFC to reduce the separation loss. Figure 4 shows the measurement results at an analysis frequency from 5 MHz to 45 MHz, without the electronic noise corrected. Here, two BHDs are switched into broadband mode, which inevitably decreases the clearance between the shot noise and electronic noise, then degrades the measured correlation noise. The entanglement bandwidth can be defined as the spectral width over which the correlation noise variance increases from its lowest variance V at small Fourier frequencies to $V + 0.5\ (1 - V)$ [41]. By definition, all of the six pairs of entangled sideband modes have a bandwidth of more than 32 MHz, which is of vital importance for high-efficiency frequency-multiplexing quantum communication. The degradation of the measured entanglement degree with the Fourier frequency is mainly attributed to the limited bandwidth of the OPO and BHDs. In future, the entanglement bandwidth can be improved by optimizing the OPO and BHDs.

Further, we measure the optimal correlation noise variances of the first- to sixth-order entangled sideband modes by employing narrowband and high-gain BHDs. Here, the BHDs have a clearance of 25 dB at 1 MHz, which corresponds to an equivalent loss of 0.33% [42]. Thus, the influence of the electronic noise on the measured results can be neglected. Figure 5 presents the measured results at an analysis frequency of 1 MHz. The entanglement degree of the first- to fifth-order entangled sideband modes is approximately 8.0 dB. The slight difference of entanglement degree with order number n mainly comes from the separation efficiency of the RFC. The sixth-order entangled sideband modes have an entanglement degree of about 6.1 dB, which is obviously less than that of the first- to fifth-order entangled sideband modes. It should be noted that the degradation of the entanglement degree is not due to the parametric process. At a modulation frequency of $\Omega_n = 6 \times \mathrm{FSR}_{\mathrm{OPO}}$, there is a smaller signal amplitude for the RF source, a lower modulation efficiency, which limits the clearance of the BHDs. Therefore,

the measured entanglement degree severely deviates from the generated value.

In summary, we have experimentally demonstrated six pairs of entangled sideband modes by employing a broadband RFC to separate the upper and lower sideband modes of one squeezed light field. Owing to the additional phase delay originating from the transmission process of the RFC, the generated sideband entanglement states have a limited bandwidth. We confirm the dependence of the time delay T on the Q factor of the RFC and propose a compensation scheme based on electronic delay. Exploiting the electronic delay compensation scheme, the bandwidth of independent entangled sideband modes is expanded to dozens of megahertz. Compared with the existing experimental demonstration scheme of entangled sideband mode detection which focuses on a single analysis frequency or minor bandwidth of several megahertz [23,24,34,35], our results represent a considerable improvement in bandwidth and channel numbers. At the same time, the maximum entanglement degree reaches 8.1 dB.

We expect to construct and detect entangled sideband modes with more channels, utilizing a new generation scheme of frequency-shifting LOs [43], or all-optical cavity enhanced parametric homodyne detection [44,45]. The quantum resource promises to provide a solution for the increase of communication capacity in a practical quantum communication system.

Funding. National Natural Science Foundation of China (62225504, 62027821, 62035015, U22A6003, 12174234, 12274275); National Key Research and Development Program of China (2020YFC2200402); Program for Sanjin Scholar of Shanxi Province.

Disclosures. The authors declare no conflicts of interest.

Data availability. Data underlying the results presented in this paper are not publicly available at this time but may be obtained from the authors upon reasonable request.

REFERENCES

1. K. Mattle, H. Weinfurter, P. G. Kwiat, and A. Zeilinger, Phys. Rev. Lett. **76**, 4656 (1996).
2. S. L. Braunstein and P. van Loock, Rev. Mod. Phys. **77**, 513 (2005).
3. H.-K. Lo, M. Curty, and B. Qi, Phys. Rev. Lett. **108**, 130503 (2012).
4. F. Grosshans, G. V. Assche, J. Wenger, R. Brouri, N. J. Cerf, and P. Grangier, Nature **421**, 238 (2003).
5. N. Wang, S. Du, W. Liu, X. Wang, Y. Li, and K. Peng, Phys. Rev. Appl. **10**, 064028 (2018).
6. S. L. Braunstein and H. J. Kimble, Phys. Rev. Lett. **80**, 869 (1998).
7. D. Bouwmeester, J.-W. Pan, K. Mattle, M. Eibl, H. Weinfurter, and A. Zeilinger, Nature **390**, 575 (1997).
8. S. Pirandola, J. Eisert, C. Weedbrook, A. Furusawa, and S. L. Braunstein, Nat. Photonics **9**, 641 (2015).
9. B. Korzh, C. C. W. Lim, R. Houlmann, N. Gisin, M. J. Li, D. Nolan, B. Sanguinetti, R. Thew, and H. Zbinden, Nat. Photonics **9**, 163 (2015).
10. S. Wengerowsky, S. K. Joshi, F. Steinlechner, H. Hübel, and R. Ursin, Nature **564**, 225 (2018).
11. S. K. Joshi, D. Aktas, S. Wengerowsky, M. Lončarić, S. P. Neumann, B. Liu, T. Scheidl, G. Currás-Lorenzo, Ž. Samec, L. Kling, A. Qiu, M. Razavi, M. Stipčević, J. G. Rarity, and R. Ursin, Sci. Adv. **6**, eaba0959 (2020).
12. Y. Chen, S. Liu, Y. Lou, and J. Jing, Phys. Rev. Lett. **127**, 093601 (2021).
13. H. Vahlbruch, M. Mehmet, K. Danzmann, and R. Schnabel, Phys. Rev. Lett. **117**, 110801 (2016).
14. J. Zhang, Phys. Rev. A **67**, 054302 (2003).
15. W. Li, X. Yu, and J. Zhang, Opt. Lett. **40**, 5299 (2015).
16. T. Kashiwazaki, N. Takanashi, T. Yamashima, T. Kazama, K. Enbutsu, R. Kasahara, T. Umeki, and A. Furusawa, APL Photonics **5**, 036104 (2020).
17. A. E. Dunlop, E. H. Huntington, C. C. Harb, and T. C. Ralph, Phys. Rev. A **73**, 013817 (2006).
18. R. Yang, J. Zhang, S. Zhai, K. Liu, J. Zhang, and J. Gao, J. Opt. Soc. Am. B **30**, 314 (2013).
19. C. Schori, J. L. Sørensen, and E. S. Polzik, Phys. Rev. A **66**, 033802 (2002).
20. M. Pysher, Y. Miwa, R. Shahrokhshahi, R. Bloomer, and O. Pfister, Phys. Rev. Lett. **107**, 030505 (2011).
21. M. Chen, N. C. Menicucci, and O. Pfister, Phys. Rev. Lett. **112**, 120505 (2014).
22. J. Roslund, R. M. de Araújo, S. Jiang, C. Fabre, and N. Treps, Nat. Photonics **8**, 109 (2014).
23. B. Hage, A. Samblowski, and R. Schnabel, Phys. Rev. A **81**, 062301 (2010).
24. S. Shi, L. Tian, Y. Wang, Y. Zheng, C. Xie, and K. Peng, Phys. Rev. Lett. **125**, 070502 (2020).
25. J. Mizuno, K. Wakui, A. Furusawa, and M. Sasaki, Phys. Rev. A **71**, 012304 (2005).
26. A. M. Marino, R. C. P. , V. Boyer, and P. D. Lett, Nature **457**, 859 (2009).
27. Y. Ma, H. Miao, B. H. Pang, M. Evans, C. Zhao, J. Harms, R. Schnabel, and Y. Chen, Nat. Phys. **13**, 776 (2017).
28. G. Hétet, B. C. Buchler, O. Glöckl, M. T. L. Hsu, A. M. Akulshin, H. A. Bachor, and P. K. Lam, Opt. Express **16**, 7369 (2008).
29. W. Yang, S. Shi, Y. Wang, W. Ma, Y. Zheng, and K. Peng, Opt. Lett. **42**, 4553 (2017).
30. S. Shi, Y. Wang, L. Tian, J. Wang, X. Sun, and Y. Zheng, Opt. Lett. **45**, 2419 (2020).
31. T. Eberle, V. Händchen, and R. Schnabel, Opt. Express **21**, 11546 (2013).
32. W. Zhang, N. Jiao, R. Li, L. Tian, Y. Wang, and Y. Zheng, Opt. Express **29**, 24315 (2021).
33. Y. Zhou, X. Jia, F. Li, C. Xie, and K. Peng, Opt. Express **23**, 4952 (2015).
34. E. H. Huntington, G. N. Milford, C. Robilliard, T. C. Ralph, O. Glöckl, U. L. Andersen, S. Lorenz, and G. Leuchs, Phys. Rev. A **71**, 041802 (2005).
35. L. Tian, S. Shi, Y. Li, Y. Wu, W. Li, Y. Wang, Q. Liu, and Y. Zheng, Opt. Lett. **46**, 3989 (2021).
36. S. Ast, R. M. Nia, A. Schönbeck, N. Lastzka, J. Steinlechner, T. Eberle, M. Mehmet, S. Steinlechner, and R. Schnabel, Opt. Lett. **36**, 3467 (2011).
37. X.-Y. Cui, Q. Shen, M.-C. Yan, C. Zeng, T. Yuan, W.-Z. Zhang, X.-C. Yao, C.-Z. Peng, X. Jiang, Y.-A. Chen, and J.-W. Pan, Opt. Lett. **43**, 1666 (2018).
38. S. Shi, Y. Wang, W. Yang, Y. Zheng, and K. Peng, Opt. Lett. **43**, 5411 (2018).
39. S. E. Hosseini, A. Karimi, and S. Jahanbakht, Opt. Commun. **407**, 349 (2018).
40. G. Lenz, B. Eggleton, C. Madsen, and R. Slusher, IEEE J. Quantum Electron. **37**, 525 (2001).
41. M. Mehmet, H. Vahlbruch, N. Lastzka, K. Danzmann, and R. Schnabel, Phys. Rev. A **81**, 013814 (2010).
42. X. Jin, J. Su, Y. Zheng, C. Chen, W. Wang, and K. Peng, Opt. Express **23**, 23859 (2015).
43. H. Vahlbruch, S. Chelkowski, B. Hage, A. Franzen, K. Danzmann, and R. Schnabel, Phys. Rev. Lett. **97**, 011101 (2006).
44. N. Takanashi, A. Inoue, T. Kashiwazaki, T. Kazama, K. Enbutsu, R. Kasahara, T. Umeki, and A. Furusawa, Opt. Express **28**, 34916 (2020).
45. Y. Tian, X. Sun, Y. Wang, Q. Li, L. Tian, and Y. Zheng, Opt. Lett. **47**, 533 (2022).